AGU PUBLICATIONS

Geophysical Research Letters

RESEARCH LETTER
10.1002/2017GL074282

Key Points:
- Normal closure of stimulated fractures after the termination of injection enhances postinjection seismicity
- Processes are strongly affected by the complex structure of three-dimensional fracture networks
- Consistent with microseismic data analyses, our simulations show that seismic events occur at the rim of the stimulation region

Supporting Information:
- Supporting Information S1
- Data Set S1
- Data Set S2
- Movie S1

Correspondence to:
E. Ucar,
eren.ucar@uib.no

Citation:
Ucar, E., Berre, I., & Keilegavlen, E. (2017). Postinjection normal closure of fractures as a mechanism for induced seismicity. *Geophysical Research Letters*, *44*, 9598–9606. https://doi.org/10.1002/2017GL074282

Received 23 MAY 2017
Accepted 14 SEP 2017
Accepted article online 18 SEP 2017
Published online 4 OCT 2017

Postinjection Normal Closure of Fractures as a Mechanism for Induced Seismicity

E. Ucar[1], I. Berre[1,2], and E. Keilegavlen[1]

[1]Department of Mathematics, University of Bergen, Bergen, Norway, [2]Christian Michelsen Research, Bergen, Norway

Abstract Understanding the controlling mechanisms underlying injection-induced seismicity is important for optimizing reservoir productivity and addressing seismicity-related concerns related to hydraulic stimulation in Enhanced Geothermal Systems. Hydraulic stimulation enhances permeability through elevated pressures, which cause normal deformations and the shear slip of preexisting fractures. Previous experiments indicate that fracture deformation in the normal direction reverses as the pressure decreases, e.g., at the end of stimulation. We hypothesize that this normal closure of fractures enhances pressure propagation away from the injection region and significantly increases the potential for postinjection seismicity. To test this hypothesis, hydraulic stimulation is modeled by numerically coupling flow in the fractures and matrix, fracture deformation, and matrix deformation for a synthetic reservoir in which the flow and mechanics are strongly affected by a complex three-dimensional fracture network. The role of the normal closure of fractures is verified by comparing simulations conducted with and without the normal closure effect.

1. Introduction

Enhanced Geothermal System (EGS) technology is considered key to unlocking geothermal energy resources because it can allow for the production of geothermal energy resources that are less dependent on initial hydrogeological conditions. An EGS can be created by hydraulically stimulating the reservoir to enhance permeability and achieve commercial flow rates. The elevated pressures activate preexisting fractures by decreasing the frictional resistance, which may lead to shear failure of the fractures depending on the fracture orientation relative to the direction and strength of the background stress anisotropy. Following shearing, the dilation of the fractures occurs in the normal direction of the fracture surfaces, which results in a permanent increase in the fracture permeability. Such a treatment is called shear dilation stimulation (which is also known as shear stimulation, hydroshearing, or low-pressure stimulation). As long as the elevated pressures are below the minimum principal stress, shear dilation remains a dominant mechanism for fracture opening (Pine & Batchelor, 1984).

Hydraulic stimulation is essential for geothermal development in low-permeability formations, such as crystalline basement rocks. However, excessive induced seismicity is a by-product observed in many EGS projects (Majer et al., 2007). Concerns related to induced seismicity can lead to the termination of costly projects, which was observed for the Basel geothermal project (Häring et al., 2008), or cause unfavorable public perception (Majer et al., 2007). These concerns provide additional motivation to identify and understand the controlling mechanisms underlying the stimulation process and incorporate these mechanisms in modeling approaches.

Fluid injection causes elevated pressures inside the fractures and reduces contact forces, resulting in decreased frictional resistance between the fracture surfaces. These changes facilitate shear slip in fractures that are favorably oriented in the anisotropic background stress field. This mechanism is known as effective stress reduction and has been identified as the major cause of induced seismicity in numerous modeling studies (Bruel, 2007; Kohl & Mégel, 2007; Rothert & Shapiro, 2003). The importance of stress redistribution following the shearing of rock for injection-induced seismicity has been emphasized (Catalli et al., 2016, 2013), and the stress alteration has been coupled with the fluid flow in several models (Baisch et al., 2010; McClure & Horne, 2011). As mentioned by Baisch et al. (2010), the stress change in the reservoir caused by slip must be included in numerical modeling because the concentration of shear stress ahead of an earthquake rupture front can cause further propagation of seismicity; hence, slip avalanches can be initiated.

Particular geothermal fields, such as Soultz-sous-Forêts, Basel, and Paralana, provide interesting examples of induced seismicity because large-magnitude events occurred in the shut-in period of the hydraulic stimulations, which is the period after fluid injection has been terminated (Albaric et al., 2014; Evans et al., 2005; Häring et al., 2008). In related modeling studies, postinjection events have been associated with the continuation of pressure diffusion and stress redistribution in the domain (Baisch et al., 2010; McClure & Horne, 2011). Recently, McClure (2015) examined a scenario where fluid backflows from highly pressurized fractures to fractures with lower pressure conditions resulted in increased postinjection seismicity. Although these previous studies provided insight in the physics of postinjection seismicity, additional effects remain to be investigated.

The seismic recordings of the Basel and Paralana geothermal projects show that the locations of seismic events after the termination of injection are mainly at the outer rim of the previous seismic activity, i.e., the stimulation region (Albaric et al., 2014; Häring et al., 2008; Mukuhira et al., 2017). Here we analyze a novel hypothesis that pertains to the mechanism underlying elevated postinjection events occurring at the boundaries of the stimulation region. The hypothesis is motivated by experiments conducted by Bandis et al. (1983) and Barton et al. (1985), who demonstrated fracture deformation under different stress conditions. Depending on the stress state, fracture deformation takes various forms, such as normal closure, opening, shearing, and dilation. The fluid pressure in the fractures has been shown to determine the normal loading on the fractures and thus the void space, or the aperture. Although the elevated pressure increases the aperture during injection, the opposite effect occurs after the injection is terminated. As the fracture starts to close, the aperture decreases, which primarily occurs in the near-well region. Our hypothesis is that a reduction in aperture will act as a postinjection pressure support to advance the front of the elevated fluid pressure and cause seismic events and a corresponding increase in apertures beyond the previously stimulated region, which was observed in the seismic recordings of Basel and Paralana. To qualify the effect of the normal closure of fractures in the postinjection phase, we examine two scenarios with and without the normal closure mechanism included after the termination of the injection.

2. Modeling and Simulation Approach

2.1. Modeling of Fracture Deformation

The fractured reservoir rock is modeled as a combination of high-permeability fractures and a porous medium surrounding the fractures, i.e., a low-permeability rock matrix. In computational modeling, the treatment of the fractures is crucial because the physical processes are controlled by the structural patterns of the fracture system. The fluid flow is dominated by the fractures as their permeability is significantly higher than that of the rock matrix. Moreover, although the rock matrix can be considered an elastic material that linearly deforms (Jaeger et al., 2007), Bandis et al. (1983) and Barton et al. (1985) showed that the fractures are more deformable than the rock matrix and should not be modeled as a linearly elastic medium. The fracture deformation is instead modeled by the Barton-Bandis closure model (Bandis et al., 1983; Barton et al., 1985), which defines the relationship between normal loading, σ_n, and fracture closure, ΔE_{rev}, as follows:

$$\sigma_n = \frac{K_n^{'}\,\Delta E_{\mathrm{rev}}}{1-\frac{\Delta E_{\mathrm{rev}}}{\Delta E_{\mathrm{max}}}}, \tag{1}$$

where $K_n^{'}$ is the initial normal stiffness per area and ΔE_{max} is the maximum possible closure. For simplicity, we take K_n to be the normal stiffness of fractures, which is considered to be constant and equal to the initial normal stiffness. Considering that the fracture network is under compression and stress is defined as positive for compression, the normal loading in a pressurized fracture is defined as the "effective normal loading", which is equal to the difference between the normal stress on the fracture and the pressure inside. Thus, the hyperbolic relationship between the effective normal stress and the fracture closure (equation (1)) is used to determine the reversible deformation depending on the pressure inside the fracture.

The pressurization of the fractures reduces the frictional resistance and ultimately leads to fracture slip in the shear direction. In the present model, the Mohr-Coulomb criterion is used to estimate the shear failure of the fractures according to a friction coefficient initially corresponding to the static friction, μ_s. After a fracture element has failed, its corresponding friction coefficient is reduced to a dynamic friction coefficient, μ_d. The

shear stress is released by a permanent shear displacement along the fracture surfaces that are exposed to shear failure. The shear displacement can be calculated by the excess shear stress concept (Rahman et al., 2002). The excess shear stress, $\Delta\tau$, is defined as the difference between the shear strength and shear stress on the fractures,

$$\Delta\tau = \tau - \mu_d \sigma_n, \tag{2}$$

where τ is the shear stress. For fracture faces that violate the Mohr-Coulomb criterion, the shear displacement, u, can be approximated by dividing the excess shear stress by the shear stiffness, $K_s^{'}$, such as in linear elastic theory:

$$u = \frac{\Delta\tau}{K_s^{'}}. \tag{3}$$

For simplicity, the shear stiffness of the fractures is taken to be constant in the following. The static/dynamic friction model falls into the category of an "inherently discrete model" because the strength of the failing elements drops discontinuously with the slip (Rice, 1993). Furthermore, sliding velocity is not resolved in static/dynamic simulations, and it is not possible to discern between slip that accumulates while sliding at seismic velocities and aseismic slip. Nevertheless, the model has been reported to provide qualitatively acceptable results (McClure, 2015; McClure & Horne, 2011).

To describe the strength of the seismicity, the shear displacements and the fracture face areas that experience shear displacements are correlated to the seismic moment, M_0:

$$M_0 = \int_A Gu\, dA, \tag{4}$$

where G is the shear modulus and A is the fracture area associated with the shear displacement.

When the fracture faces start to slip, the characteristics of the opposing fracture surfaces are altered due to the asperity damage, which takes the form of irreversible increments in the void space (Barton et al., 1985). For flow simulation purposes, the void space between fracture faces is set to be equal to the mechanical aperture and calculated by considering fracture deformations and the mechanical aperture of the initial state. The final form of the mechanical aperture, E, can be written as

$$E = E_0 - \Delta E_{\text{rev}} + \Delta E_{\text{irrev}}, \tag{5}$$

where E_0 is the initial state, calculated under zero stress conditions, and ΔE_{irrev} is the irreversible dilation of the fracture due to the shear slip, which is calculated by multiplying the tangent of the dilation angle, φ_{dil}, by the slip in the shear direction, u.

The permeability of the fracture is linked to the hydraulic aperture between fracture surfaces, e, by a cubic law (Jaeger et al., 2007). The hydraulic aperture depends on several parameters, such as the roughness, tortuosity, and contacts between the fracture surfaces. These effects are lumped into the "joint roughness coefficient" (JRC) in the relationship.

$$e = \frac{E^2}{\text{JRC}^{2.5}}, \tag{6}$$

where E and e both have the units of μm (Barton et al., 1985). Equation (6) is only valid for $E \geq e$ (Barton et al., 1985), and in practice, a maximum threshold, E_{max}, must be enforced. JRC values can be obtained experimentally or via comparisons between the observed fracture surfaces and previously measured fracture surfaces (Barton & Choubey, 1977).

Although the elevated pressure results in an increase of the mechanical aperture in the injection phase, the opposite effect occurs during the postinjection phase according to equations (1) and (5) because of the

reversibility of ΔE_{rev}. As the mechanical aperture of a fracture is correlated with its permeability, the pressure drop around the injection region after the termination of the well reverses (to some extent) the increased permeability provided by the injection phase. Because the void space is reduced compared with the situation in the injection phase, the mechanical deformations around the well decrease the effective storage capacity and push the pressure front further, thereby causing additional seismic activity.

2.2. Multiphysics Coupling

Prior to the hydraulic stimulation, the reservoir is assumed to be stable under in situ conditions. The fractures are described as two surfaces that stay in contact (the effective normal loading is greater than zero) but still permit fluid flow because of microscale surface roughness. Our model includes fluid flow in the fractures and matrix, fracture deformation, and rock matrix deformation as well as the coupling of these three processes.

The modeled stimulation process is conducted by the injection of an isothermal, single-phase, slightly compressible fluid. The fluid flow is governed by mass balance and Darcy's law both in the fractures and the matrix. Implicit time discretization is used for the time derivative in the governing equations. The computational grid conforms to the fractures and is constructed using Gmsh (Geuzaine & Remacle, 2009). For the spatial discretization, the flow equations are approximated by a cell-centered finite volume method, specifically, the two-point flux approximation (TPFA). The fracture flow and fracture-matrix interaction are modeled by a discrete fracture matrix (DFM) approach as implemented in the MATLAB Reservoir Simulation Toolbox (MRST) (Lie et al., 2012). The DFM models (Karimi-Fard et al., 2003; Sandve et al., 2012) enable the modeling of reservoir fluid flow because dominant fractures are explicitly represented in an otherwise low-permeability rock. The region surrounding the explicitly represented fracture network accounts for low but nonnegligible flow in the pores and small-scale fractures.

The shear displacements induced by the fluid injection result in stress alterations and deformations in the rock matrix. The perturbations in the stress state are governed by the equations of quasi-static equilibrium with negligible body forces, whereas the weight of the overburden is accounted for by the background stress conditions. The matrix is assumed to be a linear elastic body with fractures represented as predefined slit-like discontinuities. It is assumed that any perturbation caused by the shear displacements immediately propagates across the domain. The poroelastic effects in the matrix are neglected, and the fluid pressure on the fracture walls is coupled with the mechanical deformation. We use a recently developed cell-centered finite volume method, multipoint stress approximation (MPSA) (Keilegavlen & Nordbotten, 2017; Nordbotten, 2014), to approximate the solution of the linear momentum balance equation because it enables the use of the same data structure applied in the fluid flow discretization. MPSA also provides the efficient inclusion of fractures by modeling them as two-dimensional surfaces linking to the matrix through internal boundary conditions, including fracture deformations in both the normal direction (change in the mechanical aperture) and the shear direction (caused by excess shear stress) (Ucar et al., 2016).

To couple the fluid flow, fracture deformation and rock matrix deformation, a two-stage procedure is applied for each time step. First, the dynamics of the mechanical aperture change associated with the pressure and the mutual response of the rock matrix is captured. This involves iterations that sequentially update pressure, reversible mechanical deformation, ΔE_{rev}, and matrix deformation. The iteration is terminated when the convergence of mechanical aperture is obtained. After the convergence of this iteration, the second stage captures the shear displacements of the fractures and the corresponding mechanical response of the matrix, which is assumed to be instantaneous relative to the fluid flow. First, the Mohr-Coulomb criterion is checked for each fracture face. These shear displacements result in an irreversible contribution to the fracture deformation ΔE_{irrev}. The mechanical response of the matrix to this fracture deformation is then calculated. Because of the stress alteration caused by the shear displacements, the Mohr-Coulomb criterion is rechecked for possible additional induced shear displacements, which are referred to as "shear avalanches" (Baisch et al., 2010). The Mohr-Coulomb criterion check is conducted until stress alterations caused by slip no longer induce additional displacements. The solution process then continues with the next time step. The solution strategy for each time step is illustrated in Figure S1 in the supporting information. Moreover, the details of the hydraulic stimulation modeling can be found in Ucar et al. (2017).

3. Simulation Study

Two three-dimensional case studies were designed to investigate the effect of the postinjection normal closure of fractures on the induced seismicity. The first case considers a reservoir with a single fracture, while the second case focuses on a reservoir that includes a complex fracture network.

3.1. Simulation Setups

For the first case (case 1), a single fracture with a 1500 m diameter was examined. The fracture had an angle of 36° from the maximum horizontal principal stress direction and a 70° dip angle. The mechanical aperture under zero-stress conditions, E_0, was set as 2.25e−4 m, and the time step was 450 s. The injection started at a rate of 1.5e−5 kg/s and increased at each time step to 7.5e−5 kg/s, 4.2e−4 kg/s, and 7e−4 kg/s. The seismic moment release after a half-hour injection was examined. For the second case (case 2), a connected fracture network with 20 fractures of diameters ranging between 500 m and 1500 m was assessed. This network can be considered to represent a subset of the fractures in a reservoir. The geometric details of the fracture network can be found in Table S1 in the supporting information. The mechanical aperture under zero-stress conditions, E_0, was set as 2e−4 m except for the fracture that included the source term, where a higher E_0 of 9e−4 m was used to allow for higher injection amounts. The same time step used in case 1 (i.e., 450 s) was applied. The injection started at a rate of 1 kg/s and increased at successive time steps of 2 kg/s, 3 kg/s, and 3 kg/s. For simplicity, the injection well was modeled as a source term inside a fracture. Because the injection was conducted from the small volume of a single source cell to a limited number of fractures and a low-permeability matrix, low injection rates were used to avoid exceeding the minimum principal stress. For these conditions, the fluid flow mainly occurred in the fractures, while leakage into the matrix was not neglected for either case.

The remaining parameters were common to both simulations and are listed in Table S2 in the supporting information. The selected computational domains were sufficiently large so that the boundary effects were negligible. In both cases, the computational grid was constructed with an unstructured tetrahedron mesh consisting of approximately 40,000 cells and the fractures were discretized using approximately 10,000 triangles. Thus, the single-fracture case has a finer grid. We used different mesh sizes in our simulations to show the normal closure effect for different grid sizes and avoid the high computational costs associated with the larger fracture network.

For both of the fracture networks, the effect of the normal closure of the fractures was analyzed by conducting stimulation scenarios with and without the inclusion of the normal closure of the fractures after the termination of the injection. While one simulation scenario applied the modeling approach described above, the other kept ΔE_{rev} constant in the postinjection period so that only the normal deformation occurred through shear dilation, ΔE_{irrev}. Notably, if the normal closure effect was eliminated from the beginning of the injection, almost all characteristics (pressure distribution, fracture permeability/porosity, and stress conditions) of the compared systems would differ significantly when the injection stopped. Therefore, we kept the scenarios identical for the injection phase to ensure a fair comparison of the results, and the normal closure effect was only isolated in the postinjection phase.

3.2. Case 1: Single Fracture

In this case, the mechanical aperture change and the postinjection seismicity of the single fracture were examined with and without the normal closure effect. Figure 1 depicts the spatial distribution of the mechanical aperture change and the seismicity of the fracture during and after the injection phase. At the end of the injection, the mechanical aperture change was highest at the injection cell and slowly decreased toward the boundary of the stimulated region. Figure 1b shows the change in the mechanical aperture after the shut-in of the well when the aperture is allowed to change because of the normal closure. The darker region in the middle shows negative changes in the mechanical aperture, which indicates that the fracture closure was caused by the pressure decrease around the well. Figure 1c illustrates the mechanical aperture change in the simulation scenario when the fracture was not allowed to close after the shut-in of the well. The middle region in this figure shows no change in the mechanical aperture. A comparison of Figures 1b and 1c clearly shows the effect of the normal closure. The region of the increased mechanical aperture was wider for the case that included normal closure (Figure 1b) because of the extra fluid flow caused by the decreased effective storage capacity in the center region. Moreover, Figure 1d shows the seismic moment rate for considered

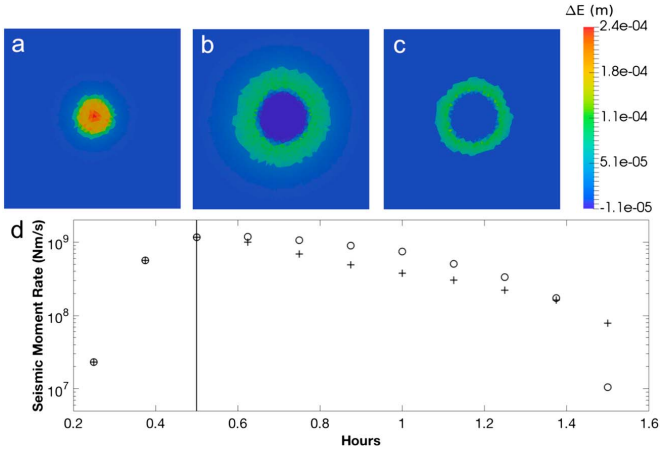

Figure 1. Normal closure behavior of the single-fracture case. Mechanical aperture changes that accumulated during (a) injection, (b) postinjection with the normal closure effect, and (c) postinjection without the normal closure effect. (d) The seismic moment rate during entire simulation. Circles and crosses show the modeled seismicity with and without the normal loading effect, respectively. The black solid line indicates the time for the termination of the injection.

simulation scenarios. Both scenarios created the same seismicity for the injection phase, as modeled. However, the normal closure effect induced a higher seismic moment rate in the postinjection phase. This difference was the direct result of the enhanced propagation of the pressure front by the normal closure of the fracture, which again decreased the frictional resistance over a wider area, thereby creating additional seismicity. Following findings of McClure and Horne (2011), the seismic moment rate started to decrease after the termination of the injection for the case which ignores the closure effect. However, the normal closure effect caused slight increase, 1.62e+7 Nm/s, in the seismic moment rate between the time step after and before the termination of injection. This observation is in line with observations by Segall and Lu (2015). The total seismic moments generated during the entire simulation with and without the normal closure effect were calculated as 2.99e+12 Nm and 2.28e+12 Nm, respectively.

3.3. Case 2: Complicated Fracture Network

The normal closure effect in a complicated three-dimensional fracture network was also examined with and without eliminating the fracture closure after the termination of the injection, as in case 1. The main results of these simulations, which are the mechanical aperture change, seismic moment rate integrated over the entire fracture network and the seismic moment rate for each time step throughout the simulation for each fracture, are presented in Figure 2. The spatiotemporal characteristics of induced seismicity with mechanical aperture changes are also provided in Movie S1 in the supporting information. The highest aperture changes are observed at the fracture where the injection is occurring, which is located in the approximate middle of the domain. We refer to this fracture as the "main fracture" (marked with a circle in Figures 2a, 2b, and 2d for clarity). The postinjection mechanical aperture change of the main fracture for the case without normal closure was positive, while for the case with normal loading, it was negative, which was expected. As seen in the Figures 2a and 2b, this resulted in higher aperture for the case without the normal loading effect than the case with the normal loading effect. For the case with normal closure, the change in the mechanical apertures achieved a peak value immediately before the injection stopped and then decreased after the termination of the injection. The shut-in of the injection source caused a pressure decrease primarily around the injection region (in other words, in the main fracture), which reduced the effective storage capacity and caused an additional flux and advancement of the pressure front. These changes created significant induced seismicity for fractures far from the injection source, which is consistent with the observed seismicity in the Basel and Paralana geothermal fields (Albaric et al., 2014; Häring et al., 2008). Because a complex fracture network

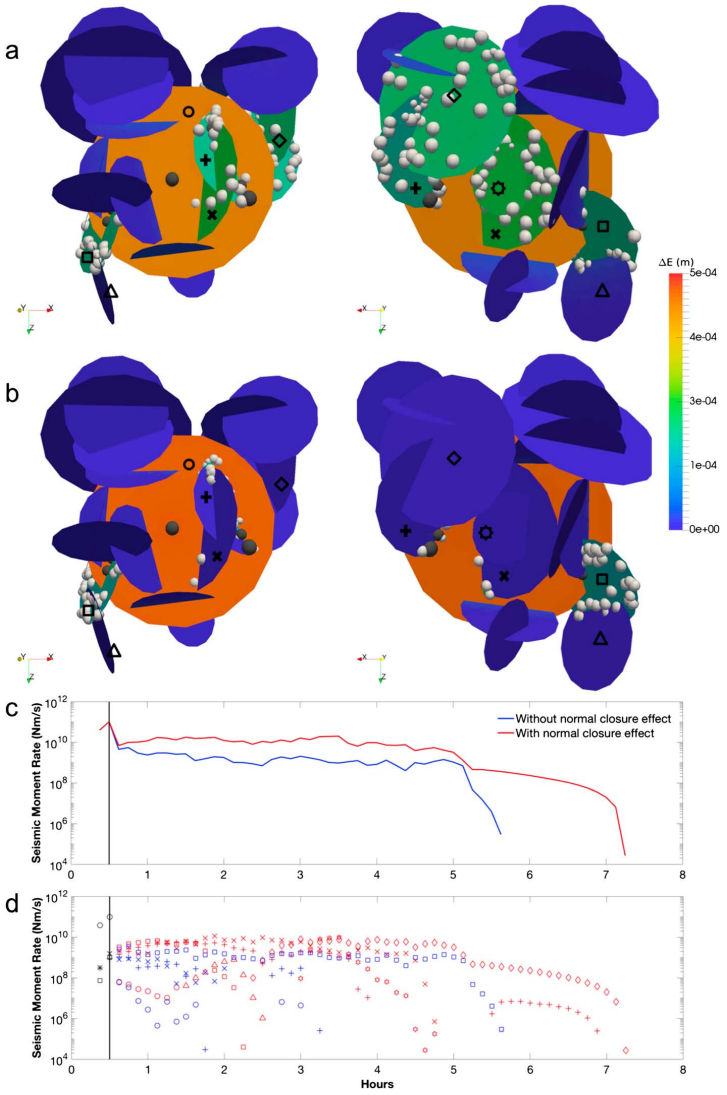

Figure 2. Seismicity and mechanical aperture change (ΔE) in a complicated fracture network. Two different views of generated seismicity: (a) with the normal loading effect and (b) without the normal loading effect. The spheres, which are associated with the seismic moment rates, are located on the faces where the largest displacement occurred for each fracture. The radiuses of the spheres are proportional with the magnitude of the seismic moment rates the entire fracture. The gray spheres show the seismicity that occurred during the injection phase, and the white spheres indicate the seismicity that occurred after the termination of the injection. (c) The seismic moments rates integrated over the entire fracture network. (d) The seismic moment rates for each fracture in each time step throughout the simulation. Each marker type represents a fracture as indicated in Figures 2a and 2b. Red markers show the modeled seismicity for the scenario in which the normal loading effect is included in the model after shut-in, and blue markers show the results for the scenario in which fracture closure is disregarded in the model after shut-in. The black solid line indicates the time for the termination of the injection for both Figures 2c and 2d.

that includes interactions between several fractures with completely different orientations was used, the pressure front reaches favorably oriented fractures far from the injection region. For the scenario in which the normal closure was excluded, less induced seismicity was observed because the pressure front could not reach favorably oriented fractures. The difference between the two situations in induced seismicity for the entire fracture network is shown in Figure 2c. The normal closure effect not only created a significant difference between the seismic moment rates but also has extended the duration of the period until no seismicity is observed by two hours. The total seismic moments generated during the entire simulation with and without the normal closure effect were calculated as 2.47e+14 Nm and 9.09e+13 Nm, respectively.

Figure 2d shows the seismic moment rates during the entire simulation for each fracture. Whereas the seismicity was triggered for only four fractures when the normal closure effect was disregarded, the number of fractures exposed to the induced seismicity reached seven when the normal loading effect was included. For the injection phase, induced seismicity was observed for four fractures (shown by a circle, plus, cross, and square in Figures 2a, 2b, and 2d). For the postinjection phase, the same four fractures continued to generate seismicity for the situation without normal loading. However, when the normal closure effect was included in the model, postinjection seismicity was observed for three different fractures that were not activated during injection. For example, the fracture marked by a diamond in Figure 2d started to induce seismicity almost 2 h after the termination of injection and continued to generate seismicity for 5 h. For both scenarios, certain fractures were not exposed to slip because of their orientation.

The current modeling approach enables us to analyze several fracture networks that have different characteristics, such as the number, shape and orientation of fractures and the network connectivity. Therefore, after validating the effect of the normal closure of fractures on the induced seismicity, we performed further studies to investigate seismic events that occur in the postinjection phase. The extent and magnitude of the postinjection induced seismicity were significantly dependent on the number of favorably orientated fractures, the connections among them and the hydromechanical properties of fracture network. The friction coefficient for all fractures was assumed to be identical in the results presented here, although it will differ for each fracture in a real fracture network. When we used different friction coefficients for different fractures, significantly larger seismicity were generated after the termination of injection than in the injection phase once the pressure front reached a fracture with favorable orientation and/or low friction. This effect can also be discussed in the context of delayed postinjection seismicity as observed in the Rittershoffen deep geothermal reservoir (Lengliné et al., 2017).

The current friction model limits the accuracy of the seismicity characteristics due to the discretization dependency (Rice, 1993). Furthermore, several assumptions, such as constant stiffness coefficients and the removal of poroelastic effects from the matrix as well as thermoelastic and geochemical effects limit the accuracy of the results. Formation of wing fractures is also ignored in our study, although it is considered as a possible outcome even for low pressuring scenarios because of tensile stress concentrations caused by shear failure (McClure & Horne, 2014). Finally, realistic injection rates are in the range of 10–50 kg/s (Mukuhira et al., 2017), where injected fluid is accommodated by main faults or fracture zones, as well as by networks of fine-scale fractures. Despite that assumptions in our model affect the system behavior quantitatively, more advanced models would not interfere with the identified effect caused by the normal closure mechanism during the postinjection phase of hydraulic stimulations.

4. Conclusions

The normal closure of fractures as a mechanism for induced seismicity in the postinjection phase of hydraulic stimulation is examined. Two different three-dimensional cases are studied: a reservoir with a single fracture and a complicated fracture network consisting of 20 fractures. A detailed analysis of the underlying mechanism is performed by comparing the results from numerical experiments conducted with and without the normal closure effect. A qualitative examination of the results for both types of fracture network suggests that the normal closure of fractures should be considered a significant mechanism that leads to elevated postinjection seismicity. Furthermore, the results indicate that the structure of the complex fracture network strongly affects the evolution of the induced seismicity. The spatiotemporal localization of the induced seismicity modeled in this network shows analogous characteristics with recorded seismicity from stimulation of geothermal reservoirs.

Acknowledgments
Data associated with this study are available in the supporting information. We are thankful to the Editor and the anonymous reviewers for the comments, suggestions, and corrections, which have improved the manuscript. The work was funded by the Research Council of Norway through grant 228832/E20 and Statoil ASA through the Akademia agreement.

References

Albaric, J., Oye, V., Langet, N., Hasting, M., Lecomte, I., Iranpour, K., … Reid, P. (2014). Monitoring of induced seismicity during the first geothermal reservoir stimulation at Paralana, Australia. *Geothermics*, *52*, 120–131. https://doi.org/10.1016/j.geothermics.2013.10.013

Baisch, S., Vörös, R., Rothert, E., Stang, H., Jung, R., & Schellschmidt, R. (2010). A numerical model for fluid injection induced seismicity at Soultz-sous-Forêts. *International Journal of Rock Mechanics and Mining Sciences*, *47*(3), 405–413. https://doi.org/10.1016/j.ijrmms.2009.10.001

Bandis, S., Lumsden, A., & Barton, N. (1983). Fundamentals of rock joint deformation. *International Journal of Rock Mechanics And Mining Sciences & Geomechanics Abstracts*, *20*(6), 249–268. https://doi.org/10.1016/0148-9062(83)90595-8

Barton, N., & Choubey, V. (1977). The shear strength of rock joints in theory and practice. *Rock Mechanics and Rock Engineering*, *10*(1), 1–54. https://doi.org/10.1007/BF01261801

Barton, N., Bandis, S., & Bakhtar, K. (1985). Strength, deformation and conductivity coupling of rock joints. *International Journal of Rock Mechanics and Mining Science and Geomechanics Abstracts*, *22*(3), 121–140. https://doi.org/10.1016/0148-9062(85)93227-9

Bruel, D. (2007). Using the migration of the induced seismicity as a constraint for fractured hot dry rock reservoir modelling. *International Journal of Rock Mechanics and Mining Sciences*, *44*(8), 1106–1117. https://doi.org/10.1016/j.ijrmms.2007.07.001

Catalli, F., Meier, M. A., & Wiemer, S. (2013). The role of Coulomb stress changes for injection-induced seismicity: The Basel enhanced geothermal system. *Geophysical Research Letters*, *40*, 72–77. https://doi.org/10.1029/2012GL054147

Catalli, F., Rinaldi, A. P., Gischig, V., Nespoli, M., & Wiemer, S. (2016). The importance of earthquake interactions for injection-induced seismicity: Retrospective modeling of the Basel Enhanced Geothermal System. *Geophysical Research Letters*, *43*, 4992–4999. https://doi.org/10.1002/2016GL068932

Evans, K., Moriya, H., Niitsuma, H., Jones, R., Phillips, W., Genter, A., … Baria, R. (2005). Microseismicity and permeability enhancement of hydrogeologic structures during massive fluid injections into granite at 3 km depth at the Soultz HDR site. *Geophysical Journal International*, *160*(1), 388–412. https://doi.org/10.1111/j.1365-246X.2004.02474.x

Geuzaine, C., & Remacle, J. F. (2009). Gmsh: A 3-D finite element mesh generator with built-in pre-and post-processing facilities. *International Journal for Numerical Methods in Engineering*, *79*(11), 1309–1331. https://doi.org/10.1002/nme.2579

Häring, M. O., Schanz, U., Ladner, F., & Dyer, B. C. (2008). Characterisation of the Basel 1 enhanced geothermal system. *Geothermics*, *37*(5), 469–495. https://doi.org/10.1016/j.geothermics.2008.06.002

Jaeger, J. C., Cook, N. G., & Zimmerman, R. (2007). *Fundamentals of Rock Mechanics*. Malden: Blackwell Publishing Ltd.

Karimi-Fard, M., Durlofsky, L. J., & Aziz, K. (2003). An efficient discrete fracture model applicable for general purpose reservoir simulators. *SPE Journal*, *9*(2), 227–236. https://doi.org/10.2118/79699-MS

Keilegavlen, E., & Nordbotten, J. M. (2017). Finite volume methods for elasticity with weak symmetry. *International Journal for Numerical Methods in Engineering*. https://doi.org/10.1002/nme.5538

Kohl, T., & Mégel, T. (2007). Predictive modeling of reservoir response to hydraulic stimulations at the European EGS site Soultz-sous-Forêts. *International Journal of Rock Mechanics and Mining Sciences*, *44*(8), 1118–1131. https://doi.org/10.1016/j.ijrmms.2007.07.022

Lengliné, O., Boubacar, M., & Schmittbuhl, J. (2017). Seismicity related to the hydraulic stimulation of GRT1, Rittershoffen, France. *Geophysical Journal International*, *208*(3), 1704–1715. https://doi.org/10.1093/gji/ggw490

Lie, K. A., Krogstad, S., Ligaarden, I. S., Natvig, J. R., Nilsen, H. M., & Skaflestad, B. (2012). Open-source MATLAB implementation of consistent discretisations on complex grids. *Computational Geosciences*, *16*(2), 297–322. https://doi.org/10.1007/s10596-011-9244-4

Majer, E. L., Baria, R., Stark, M., Oates, S., Bommer, J., Smith, B., & Asanuma, H. (2007). Induced seismicity associated with enhanced geothermal systems. *Geothermics*, *36*(3), 185–222. https://doi.org/10.1016/j.geothermics.2007.03.003

McClure, M. W. (2015). Generation of large postinjection-induced seismic events by backflow from dead-end faults and fractures. *Geophysical Research Letters*, *42*, 6647–6654. https://doi.org/10.1002/2015GL065028

McClure, M. W., & Horne, R. N. (2011). Investigation of injection-induced seismicity using a coupled fluid flow and rate/state friction model. *Geophysics*, *76*(6), WC181–WC198. https://doi.org/10.1190/GEO2011-0064.1

McClure, M. W., & Horne, R. N. (2014). An investigation of stimulation mechanisms in Enhanced Geothermal Systems. *International Journal of Rock Mechanics and Mining Sciences*, *72*, 242–260. https://doi.org/10.1016/j.ijrmms.2014.07.011

Mukuhira, Y., Dinske, C., Asanuma, H., Ito, T., & Häring, M. (2017). Pore pressure behavior at the shut-in phase and causality of large induced seismicity at Basel, Switzerland. *Journal of Geophysical Research: Solid Earth*, *122*, 411–435. https://doi.org/10.1002/2016JB013338

Nordbotten, J. M. (2014). Cell-centered finite volume discretizations for deformable porous media. *International Journal for Numerical Methods in Engineering*, *100*(6), 399–418. https://doi.org/10.1002/nme.4734

Pine, R., & Batchelor, A. (1984). Downward migration of shearing in jointed rock during hydraulic injections. *International Journal of Rock Mechanics and Mining Science and Geomechanics Abstracts*, *21*(5), 249–263. https://doi.org/10.1016/0148-9062(84)92681-0

Rahman, M., Hossain, M., & Rahman, S. (2002). A shear-dilation-based model for evaluation of hydraulically stimulated naturally fractured reservoirs. *International Journal for Numerical and Analytical Methods in Geomechanics*, *26*(5), 469–497. https://doi.org/10.1002/nag.208

Rice, J. R. (1993). Spatio-temporal complexity of slip on a fault. *Journal of Geophysical Research*, *98*, 9885–9907. https://doi.org/10.1029/93JB00191

Rothert, E., & Shapiro, S. A. (2003). Microseismic monitoring of borehole fluid injections: Data modeling and inversion for hydraulic properties of rocks. *Geophysics*, *68*(2). https://doi.org/10.1190/1.1567239

Sandve, T., Berre, I., & Nordbotten, J. M. (2012). An efficient multi-point flux approximation method for discrete fracture-matrix simulations. *Journal of Computational Physics*, *231*(9), 3784–3800. https://doi.org/10.1016/j.jcp.2012.01.023

Segall, P., & Lu, S. (2015). Injection-induced seismicity: Poroelastic and earthquake nucleation effects. *Journal of Geophysical Research: Solid Earth*, *120*, 5082–5103. https://doi.org/10.1002/2015JB012060

Ucar, E., Berre, I., & Keilegavlen, E. (2017). Three-dimensional numerical modeling of shear stimulation of naturally fractured rock formations. arXiv:1709.01847.

Ucar, E., Keilegavlen, E., Berre, I., & Nordbotten, J. M. (2016). Finite-volume discretization for the deformation of fractured media. arXiv:1612.06594.

Geophysical Research Letters

Supporting Information for

Post-injection normal closure of fractures as a mechanism for induced seismicity

E. Ucar[1], I. Berre[1, 2], and E. Keilegavlen[1]

[1] Department of Mathematics, University of Bergen, Bergen, Norway.

2 Christian Michelsen Research, Bergen, Norway.

Contents of this file

Additional Supporting Information (Files uploaded separately)

Introduction

The supporting information includes Figure S1, Table S1, Table S2, the caption for Movie S1, and the caption for datasets associated with the presented study. Figure S1 illustrates the two-stage solution procedure for each time step. The details about the solution procedure can be found in (Ucar et al., 2017). Table S1 and Movie S1 both belong to Case 2 examined in the paper. Table S1 provides details on the fracture network, and Movie S1 shows the results of the numerical experiment as a function of time. Table S2 includes the common parameters used for both Case 1 and Case 2.

The datasets regarding the presented work have been obtained with following the solution procedure mentioned in the paper and in (Ucar et al., 2017). The datasets are divided in two parts. Data Set S1 and Data Set S2 include all the data presented in the study as mesh, the mechanical aperture and the seismicity rate in each time step for Case 1 and Case 2, respectively. In Data Set S1, one can see 13 column of the mechanical aperture that each column represents each time step starting from the initial mechanical aperture distribution. Moreover, seismic moment rates have 12 rows that each represent time step starting from the end of first time step. Data Set S2 belongs to Case 2, which includes 20 fractures. Here, one can see 46 columns of data for the mechanical aperture that each column represents each time step starting from the initial mechanical aperture distribution when the normal closure effect is neglected. However, 59 columns of data for the mechanical aperture can be found when the normal closure effect is included. The numbers of the columns are different here because the data include the time steps until no more seismicity is

recorded. For seismic moment rates, the data includes 45 rows when the normal closure effect is discarded whereas it includes 58 rows when the normal closure effect included due to the same reason. Apart from rows, seismic moment rates have 20 columns here in which each column represents each fractures. It is beneficial to note that, since the solution procedure is implemented with the help of MRST, the details about the mesh structure can be found in (Lie et al., 2012).

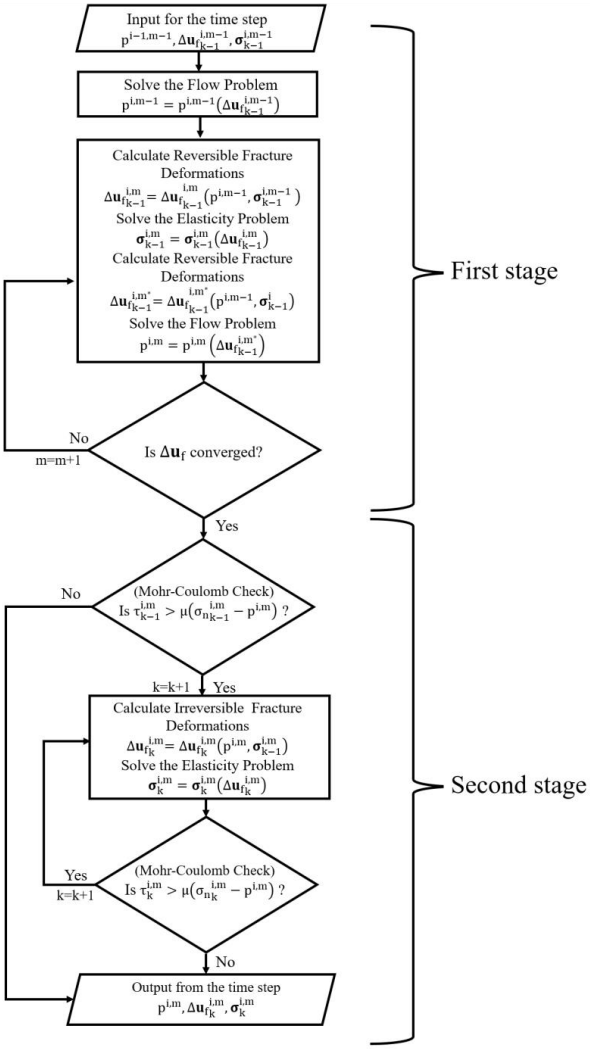

Figure S1. The two-stage solution procedure for each time step reprinted from (Ucar et al., 2017). The symbols are defined as follows: p is pressure, $\Delta\mathbf{u}_f$ is the fracture deformation, $\boldsymbol{\sigma}$ represents stress, σ_n is normal stress, τ is shear stress and μ is the friction coefficient. The $\Delta\mathbf{u}_f$ is defined as $\mathbf{n}(\Delta E_{rev} + \Delta E_{irrev}) + \mathbf{t}u$ where the unit vectors $\mathbf{n}$ is the outer normal vector of the fracture surface, $\mathbf{t}$ is the tangent vector in the direction of the shear displacement and u defines the shear displacement between the fracture surfaces. The indices in the superscript indicate the two stages of the solution procedure for each time step.

Fracture No	x (m)	y (m)	z (m)	Fracture Diameter (m)	Strike	Dip
1	0	0	-5000	1500	100	80
2	-200	-200	-4850	700	170	70
3	500	200	-5200	850	130	70
4	100	100	-5000	1000	60	80
5	-400	100	-5500	800	100	30
6	-400	300	-5000	700	170	70
7	-600	-100	-4600	700	50	70
8	-500	0	-5000	700	150	85
9	-500	0	-5700	1200	300	45
10	-400	-200	-5900	800	300	80
11	-400	-100	-5700	800	100	50
12	400	400	-5500	1000	250	85
13	-600	-100	-4200	700	220	75
14	0	0	-4400	700	300	25
15	500	200	-5800	700	300	25
16	700	100	-5800	700	100	75
17	0	300	-4300	500	150	75
18	0	300	-5000	500	120	75
19	-300	-600	-4900	700	300	25
20	-200	-900	-4900	600	30	75

Table S1. Details of the fracture network used for Case 2. The coordinates of the center of the fractures (x, y, and z) are calculated by considering the wellhead of fracture no 1 (main fracture) as the origin.

Fluid Flow Parameters	
Initial hydrostatic pressure	40 MPa
Fluid initial density	1014 kg/m^3
Fluid viscosity	1 cp
Fluid compressibility	0.000458 MPa^{-1}
Rock matrix permeability	1nD
Rock matrix porosity	0.01
Fracture Parameters	
Normal stiffness, K_n	3.5x10^{16} N/m
Shear stiffness per area, K'_s	2 GPa/m
Dilation angle	3
JRC	15
Maximum possible closure, ΔE_{max}	E_0
Friction, μ_s and μ_d	0.6 and 0.55
Maximum threshold, E_{max}	8.5e-4 m
Elastic Parameters of Rock Matrix	
Shear modulus, G	21.6 GPa
Poisson's ratio	0.25
Principal stresses (S_H, S_h, S_V)	120 MPa, 80 MPa, 100 MPa

Table S2. The common parameters used for both Case 1 and Case 2.

Data Set S1. The dataset for Case 1. This dataset includes the mesh used for this problem in data 'Mesh', the mechanical aperture for each time step in data 'E_timestep_withoutNC' when the normal closure effect is discarded, 'E_timestep_withNC' when the normal closure effect is considered. Seismic moment rates calculated in each time step in data 'SeismicMomentRate_withoutNC' when the normal closure effect is discarded, 'SeismicMomentRate_withNC'' when the normal closure effect is considered.

Data Set S2. The dataset for Case 2. This dataset includes the mesh used for this problem in data 'Mesh', the mechanical aperture for each time step in data 'E_timestep_withoutNC' when the normal closure effect is discarded, 'E_timestep_withNC' when the normal closure effect is considered. Seismic moment rates calculated in each time step in data 'SeismicMomentRate_withoutNC' when the normal closure effect is discarded, 'SeismicMomentRate_withNC'' when the normal closure effect is considered.

Movie S1. Seismicity and mechanical aperture change (ΔE) in a complicated fracture network as a function of time. Results with a normal loading effect (top) and without a normal loading effect (bottom) are shown in three different views. The spheres associated with the seismic moments are located at the faces on which the largest event occurred for each fracture. The radiuses of the spheres are proportional with the magnitude of the seismic moment rates.